THE JOURNAL OF PHYSICAL CHEMISTRY B

ARTICLE

pubs.acs.org/JPCB

Physically Motivated, Robust, ab Initio Force Fields for CO_2 and N_2

Kuang Yu, Jesse G. McDaniel, and J. R. Schmidt*

Theoretical Chemistry Institute and Department of Chemistry, University of Wisconsin, Madison, Wisconsin 53706, United States

Supporting Information

ABSTRACT: We present a novel methodology for developing physically motivated, first-principles polarizable force fields and apply these techniques to the specific cases of CO_2 and N_2. Exchange, electrostatic, induction, and dispersion interaction parameters were fit to symmetry adapted perturbation theory (SAPT) dimer energy calculations, with explicit terms to account for each of the dominant fundamental interactions between molecules. Each term is represented by a physically appropriate functional form and fitted individually based on the results of the SAPT decomposition. The resulting CO_2 and N_2 force field was benchmarked against a diverse set of experimental data, including the second virial coefficient, density, scattering structure factor, heat capacity, enthalpy of vaporization, and vapor−liquid coexistence curves. In general, excellent agreement with experimental data is obtained with our model. Due to the physical nature of their construction, these force fields are robust and transferable to environments for which they were not specifically parametrized, including gas mixtures, and we anticipate applications in modeling CO_2/N_2 adsorption in polar and/or heterogeneous media.

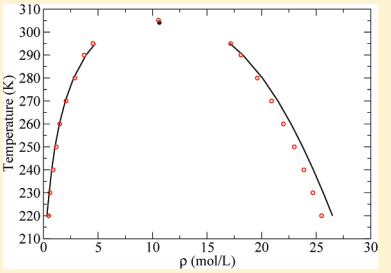

INTRODUCTION

There has been significant recent interest in understanding the properties and interactions of carbon dioxide (CO_2) due to its critical role in global warming. The growing importance of processes such as CO_2/CH_4 separation, syngas chemistry, and flue gas separation highlights the need to understand the physical interactions involving CO_2 under industrially relevant temperatures and pressures. In particular, the latter example has recently been the subject of much attention to design efficient postcombustion carbon capture and sequestration (CCS) systems for coal-fired power plants.[1] Here the primary challenge is the separation of the relatively dilute CO_2 from the more abundant nitrogen (N_2) gas, utilizing technologies such as chemical sorbants, porous materials,[2,3] or ionic liquids.[4−6] Computer simulation techniques have been applied to these areas with the goal of providing physical insight into the gas sorption and separation process.[7,8] The reliability of these techniques hinges on the accuracy of the force field used to describe both the interaction of the gas and gas/sorbent over a wide range of conditions.

In this paper we present accurate, physically motivated, ab initio force fields for CO_2 and N_2. These force fields are novel in that they are essentially parameter-free and based on extremely accurate ab initio calculations. They contain *explicit* terms to account for all of the dominant fundamental interactions between molecules (Pauli repulsion, electrostatics, induction, dispersion, ...), each represented by a physically appropriate functional form and fit *individually* to an ab initio energy decomposition. As such, the resulting force fields are extremely robust and transferable, reproducing a vast array of structural, thermodynamic, and dynamic properties over large portions of the phase diagram and for gas mixtures. We also anticipate that they will be well-suited for use in simulating CO_2 interactions in complex media such as porous solids (metal−organic frameworks, zeolites) and ionic liquids where traditional empirical force fields often struggle.

There have been a considerable number of early attempts to develop classical force fields for CO_2.[9−15] More recently, Moller et al. developed a two-center Lennard-Jones plus point quadrupole (2CLJQ) model that was carefully benchmarked to vapor−liquid phase equilibria (VLE) properties.[16] One year later, in 1995, Harris and Yung published their EPM2 model,[17] which is one of the most widely used classical models for CO_2 today. EPM2 model is a flexible model with three Lennard-Jones sites and three point charges each located on atom centers. EPM2 model yields a very accurate liquid−vapor coexistence curve and critical point, although its bond length and charges are scaled by 0.97−0.98 with respect to its precursor, EPM, which is much less accurate in phase coexistence calculations. More recently, Potoff and Siepmann developed their TraPPE model,[18] which contains a more reasonable bond length and yields comparable accuracy in VLE calculations to EPM2. Furthermore, the TraPPE model was also developed for various other species, such as N_2 and alkanes, making it a convenient choice when mixtures were simulated.

Further work has since been done to improve the description of various model properties, including a modified 2CLJQ model by Vebrec et al.,[19] a rigid three Lennard-Jones plus three charges model proposed by Zhang and Duan,[20] and a full flexible version by Zhu et al.[21] The latest work along these lines is a three Lennard-Jones sites plus point quadrupole (3LJQ) model published by Merker et al. in 2010,[22] which yields excellent agreement with experiment in various types of properties, including densities, second virial coefficients, radial distribution function, diffusion coefficients, and VLE data. But like EPM2, the authors were forced to scale the quadrupole moment and bond length by 8% to achieve high accuracy. Finally, of particular

Received: May 16, 2011
Revised: July 6, 2011
Published: July 07, 2011

note is the GCPCDO model published in 2011 by Persson which is the first model to explicitly treat three body interactions.[23] This model has one anisotropic polarizable site and three body dispersion terms, yielding improved second and third virial coefficients; many macroscopic properties including VLE data were not benchmarked, likely due to the computational expense of the model.

It is important to note that all these models were directly fit to bulk experimental data. This may lead to the occurrence of unphysical parameters in these models, and thus their accuracy often relies on some implicit error cancellation. Not only is this somewhat unsatisfying, but it also means that the model transferability is questionable. An alternative approach is to directly fit ab initio calculations.[24−27] Along these lines, Tsuzuki et al. developed a CO_2 model fit directly to interaction energies computed with MP2 level of theory.[28,29] Although they achieved a nice fit to the pairwise potential, a relatively large error in the density and diffusion coefficient was observed, and other important macroscopic properties such as VLE data were not presented. Another use of ab initio calculations was made by Bukowski et al., fitting a potential based on symmetry-adapted perturbation theory (SAPT) calculations.[30] However, they mainly focused on geometries of dimers and trimers and did not attempt to simulate bulk systems. Furthermore, in contrast to the present models, they fit only the *total* interaction energy, rather the individual energy *components*. The latter approach not only provides access to explicit energy decomposition but also, more importantly, should increase the robustness of the potential in alternative environments other than the neat fluid.

Our present goal in this work is to design a physically motivated CO_2 model based on first-principle calculations, achieving at least comparable accuracy for bulk properties as the previously mentioned empirical models. Our approach, based on a physically motivated functional form with explicit terms for each relevant fundamental interactions and fit individually to energy decomposed ab initio calculations, should yield more physical insight and better transferability and robustness than previous empirical models. Specifically, we use a combination of density fitting DFT-SAPT[31−36] and coupled cluster calculations with extremely large basis sets to compute decomposed interaction energies, which are used to fit physically distinct terms of our force field. This combination of computational approaches yields extremely accurate interaction energies along with a well-defined and physically meaningful energy decomposition.

Finally, in conjunction with our CO_2 model, a new N_2 model was constructed using an identical methodology. Although N_2 is a common component in mixtures involving CO_2, relatively less work has been done in the construction of N_2 force fields. Several existing empirical force fields can be found in the literature,[18,19,37−40] including a polarizable shell model[41] fit to experimental properties. In addition to empirical N_2 potentials, several ab initio potentials also exist, including work done by Berns et al.[42] and van der Avoird et al.,[43] although they do not perform particularly well for bulk calculations without the introduction of significant corrections. Several related pair potentials have been developed on the basis of CCSD(T),[44,45] SAPT,[46,47] or MCSCF,[48] but bulk property benchmarks for most of these models have not been carried out. Thus it appears that no entirely satisfactory, transferable, ab initio N_2 potentials have been developed. As such, we also apply our methodology to the construction of a robust, physically motivated, ab initio model for N_2. The resulting model should be useful in simulating not only neat N_2 but also common gas mixtures.

COMPUTATIONAL DETAILS

Ab Initio Calculations. All ab initio calculations were carried out using the MolPro 2009 package.[49] The density fitting DFT-SAPT[31−36] method was used to calculate all dimer interactions during parameter fitting in conjunction with the PBE exchange correlation functional.[50,51] A long-range asymptotic correction[52] was used in the DFT part of the calculation to guarantee correct asymptotic behavior of the electron density, which is essential for accurate SAPT results. The asymptotic correction requires an ionization potential for each molecular species, and these were calculated at the PBE0/AVTZ level. A dimer-centered basis set (DCBS) consisting of Dunning style aug-cc-pVQZ basis plus mid bond functions was used in all SAPT calculations. The basis was augmented with additional midbond basis functions, consisting of 5s5p3d2f even tempered basis functions (ratio of 2.5) centered at ζ = 0.5, 0.5, 0.3, 0.3 au, respectively, and placed at the midpoint between the respective centers of mass of the two molecules of the dimer. The midbond functions are essential for accurate calculation of dispersion energies.[53]

For all CCSD(T) calculations, an aug-cc-pVQZ and additional 5s3p1d1f even tempered midbond basis was used. Counterpoise corrections are conducted to remove basis set superposition error (BSSE).

Molecular Dynamics (MD) Simulations in Homogeneous Region. All MD simulations were carried out using the Gromacs 4 simulation package.[54] All simulations in the homogeneous region of the phase diagram were done with 1000 gas molecules. Electrostatic interactions were described with the particle-mesh Ewald (PME) method in conjunction with a 14 Å real space cutoff. The Buckingham component of the potential was computed using a 15 Å cutoff and long-range energy/pressure corrections. A Nose−Hoover thermostat and Parrinello−Rahman barostat were utilized for temperature and pressure coupling, with coupling times of 0.2 and 1.0 ps, respectively. A cubic box with isotropic coupling was used for *NPT* simulations, and a 1 fs time step was used for all simulations.

Chemical Potential/VLE Calculations. Test particle insertion (TPI) calculations were utilized to evaluate the chemical potential of the vapor/liquid to determine phase coexistence conditions. All TPI calculations were conducted using a custom version of the MCCCS Towhee simulation package which was modified to enable the use of polarizable models via a shell model.[55] A conjugate gradient algorithm[56] was used to optimize the shell positions. In a typical chemical potential calculation, a 1 ns *NPT* trajectory was run using Gromacs, saving snapshots every 1 ps. Then these 1000 snapshots were analyzed using Towhee with 1000 trial insertions attempted for each snapshot. The insertions utilized a rotational biasing method to enhance the sampling[57] in which ten test insertions were conducted for every trial insertion. The Buckingham potential without electrostatics was used as the biasing potential. The chemical potential of the system in the NPT ensemble is then calculated as follows:

$$\mu_{tot} = \mu_{ex} + \mu_{id}$$

$$\mu_{ex} = -kT \ln\left(\frac{\langle w(n)V \exp(-\beta(\Delta U - \Delta U_{bias}))\rangle}{n\langle V\rangle}\right)$$

$$\mu_{id} = -kT \ln\left(\frac{1}{\Lambda^3}\left\langle\frac{V}{N}\right\rangle\right)$$

where $w(n)$ is the Rosenbluth weight,[58] Λ is the thermal de Broglie wavelength, ΔU is the change in the potential energy upon trial particle insertion, and n is the number of test insertions for each trial insertion (set equal to 10).

RESULTS AND DISCUSSION

CO_2 Model Fitting. An *NVT* MD simulation was first run at high (liquid-like) CO_2 density using the TraPPE parameters to generate representative dimer configurations for further analysis. High temperatures (3000 K) were used to enhance the sampling in repulsive regions. Approximately 800 dimer configurations were randomly selected from the trajectory to be used in subsequent SAPT calculations.

SAPT naturally decomposes the interaction energy into different terms with distinct physical meaning:

$$E_{\text{int}} = E^{(1)}_{\text{pol}} + E^{(1)}_{\text{exch}} + E^{(2)}_{\text{ind}} + E^{(2)}_{\text{ind-exch}} + E^{(2)}_{\text{disp}} + E^{(2)}_{\text{disp-exch}} + E_{\delta\text{hf}}$$

Here $E^{(1)}_{\text{pol}}$ is the electrostatic interaction due to the zeroth-order (unperturbed) electron density of isolated monomers. This electrostatic term is modeled by our force field using atom centered point charges fit to the experimental gas phase quadrupole moment. Additional terms are used to account for charge penetration effects, yielding a final functional form,

$$E^{(1)}_{\text{pol}} \cong \sum_{i>j} f(r_{ij})\frac{q_i q_j}{r_{ij}} + \sum_{i>j} A^{\text{elect}}_{ij} \exp(-B_{ij} r_{ij})$$

At least for the present cases we found that we were able to eliminate the screening function, setting $f(r_{ij}) = 1$, without any significant loss of accuracy. We thus used this approximation for the remainder of the present work.

The first-order exchange repulsion term, $E^{(1)}_{\text{exch}}$, was described using pairwise additive exponential terms in the force field,

$$E^{(1)}_{\text{exch}} \cong \sum_{i>j} A^{\text{exch}}_{ij} \exp(-B_{ij} r_{ij})$$

This Buckingham functional form is more physical than the commonly used r^{-12} repulsive terms in the Lennard-Jones potential as it more accurately describes the overlap of monomer electron densities, which themselves asymptotically decay exponentially.

The polarization/induction energy components, $E^{(2)}_{\text{pol}} = E^{(2)}_{\text{ind}} + E^{(2)}_{\text{ind-exch}}$, were reproduced using a shell model.[59] In the shell model, a positive core charge (q_{core}), located at the nucleus, and a negative shell charge (q_{shell}), are added to each polarizable atom site. The total apparent charge on a polarizable site is thus $q = q_{\text{core}} + q_{\text{shell}}$. The two charges are connected by a harmonic spring, and the positions of the shells are optimized at each simulation time step to reflect the adiabatic relaxation of the electronic polarization. The difference between the energy of this optimized system and the energy of the corresponding nonpolarizable system (with shell charge localized at the nucleus) is defined as the polarization energy of the shell model, U_{shell}.

While the intramolecular shell−shell interaction is calculated, a polarization catastrophe may arise due to the short distance between polarizable sites. A screening function was proposed by Thole[60,61] and is applied to damp the intramolecular dipole−dipole interactions to avoid such a divergence. The Thole damping functions can be written as follows:

$$U_{ij} = T(r_{ij})\frac{q_i q_j}{r_{ij}}$$

$$T(r_{ij}) = 1 - \left(1 + \frac{p r_{ij}}{2(\alpha_i\alpha_j)^{1/6}}\right) e^{-p r_{ij}/(\alpha_i\alpha_j)^{1/6}}$$

where, p is a dimensionless Thole parameter and α_i, α_j are the polarizabilities of the two interacting sites, which are calculated using equation $q_{\text{shell}}{}^2/k$, where k is the spring constant. In this case, the spring constant k and the Thole parameter p were fixed to be 0.1 au and 2.0, respectively.

To fit the shell charges (equivalent to polarizabilities), we carried out SAPT calculations involving a single point charge (Li^+) and CO_2 molecule and used the resulting induction energies from these calculations for the fit. The two components of molecular polarizability derived from this fit ($\alpha_\parallel$ = 3.913 Å^3, $\alpha_\perp$ = 2.137 Å^3) are very close to experimental values[62] (4.034 and 1.927 Å^3, respectively). In addition to the shell model, an extra exponential term was used to fit the CO_2−CO_2 induction components to account for charge penetration effects. The total functional form used to model the CO_2−CO_2 induction energy is thus,

$$E^{(2)}_{\text{pol}} \cong U_{\text{shell}} + \sum_{i>j} A^{\text{ind}}_{ij} \exp(-B_{ij} r_{ij})$$

Second-order dispersion energy, $E^{(2)}_{\text{VdW}} = E^{(2)}_{\text{disp}} + E^{(2)}_{\text{disp-exch}}$, was fit using the standard r^{-6} functional form,

$$E^{(2)}_{\text{VdW}} \cong -\sum_{i>j} f(r_{ij})\frac{C_{ij}}{r_{ij}{}^6}$$

where once again we approximated $f(r_{ij}) = 1$ without significant loss of accuracy.

Finally, the delta Hartree−Fock terms, $E_{\delta\text{hf}}$, which have been used and described previously,[31] represent primarily higher order contributions to polarization and/or exchange and are typically quite small at equilibrium intermolecular distances. These energies were computed by the difference of the Hartree−Fock dimer interaction energy and the HF-SAPT interaction energy components: $E_{\delta\text{hf}} = E^{\text{HF}}_{\text{int}} - E^{(1)}_{\text{pol}} - E^{(1)}_{\text{exch}} - E^{(2)}_{\text{ind}} - E^{(2)}_{\text{ind-exch}}$. This energy was fit using simple exponential functions,

$$E_{\delta\text{hf}} \cong \sum_{i>j} A^{\delta\text{hf}}_{ij} \exp(-B_{ij} r_{ij})$$

During the fitting procedure, the CO_2 was constrained to be linear with a bond length of 1.164 Å, near to the experimental value. Only the amplitudes of the exponential functions, $\{A_{ij}\}$, were fit to SAPT interaction energies as other parameters have been fixed on the basis of physical considerations, vide infra.

Identical pairwise exponents, B_{ij}, were used for all types of energy terms, which were determined using the following procedure. First, the electron density overlap $S_{ij}(r)$ for any pair of atoms (C−C, C−O, O−O) was approximated by assuming a spherically symmetric density distribution and exponential density tail decay for each individual atom: $n(r) \rightarrow \exp[-2r(2\mu)^{1/2}]$,[63] where μ is the experimental atomic ionization potential. Then, all pairwise $S_{ij}(r)$ were fit with exponential functions to give initial guesses for all pairwise exponents B^0_{ij} under the hypothesis that the asymptotic exponential decay of many of the energy terms should be proportional to the decay in the calculated density overlap. Finally, the first-order exchange energies from CO_2−CO_2 calculations, $E^{(1)}_{\text{exch}}$, were fit using the functional form, $\Sigma_{i>j} A^{\text{exch}}_{ij} \exp(-\lambda B^0_{ij} r_{ij})$, in which a common scaling factor was obtained; in the present cases we find $\lambda \approx 1.2$, reflecting the fact that initial exponents are only asymptotically correct. Subsequently, the exponents $B_{ij} = \lambda B^0_{ij}$ were used in all remaining energy terms.

Table 1. Fitted Parameters for CO_2 Molecules[a]

k_{spring} [(kJ/mol)/Å^2]	937.72		
r_{co} (Å)	1.164		
	C	O	
q(e)	0.65738	−0.32869	
q_{shell}(e)	−0.89712	−0.77973	
	C−C	C−O	O−O
A^{tot} (kJ/mol) /10^4	5.6303	14.183	32.748
B (Å^{-1})	3.5105	3.6993	3.9288
C [kJ/(mol·Å^{-6})] /10^2	6.891	11.242	18.341
A^{elect} (kJ/mol) /10^4	−2.7847	−6.7560	−16.391
A^{exch} (kJ/mol) /10^4	9.5510	22.327	52.190
A^{ind} (kJ/mol) /10^4	−1.3425	−0.7752	−0.4476
$A^{\delta hf}$ (kJ/mol) /10^4	0.2065	−0.6124	−2.6042

[a] C coefficient in the table is scaled by 0.935, as described in the text.

The remaining exponential coefficients, $\{A_{ij}\}$, for the various energy terms are fit individually to the results of the corresponding terms in the SAPT calculation, with fixed B_{ij}, using least mean square error approach. With the exception of the delta Hartree−Fock term, we fit only *atomic* exponential coefficients, $\{A_{ii}\}$, with the cross terms (aside from the sign) being calculated using standard combination rules, $A_{ij} = (A_{ii}A_{jj})^{1/2}$. This procedure helps to ensure the most physically meaningful parameters and further reduce their number.

We can write the final total classical potential as

$$U_{tot} = \sum_{i>j} \frac{q_i q_j}{r_{ij}} + \sum_{i>j} \left(A_{ij}^{tot} \exp(-B_{ij} r_{ij}) - \frac{C_{ij}}{r_{ij}^6} \right) + U_{shell}$$

where i, j run over all three atoms in the CO_2 molecule, and $A_{ij}^{tot} = A_{ij}^{elec} + A_{ij}^{exch} + A_{ij}^{ind} + A_{ij}^{\delta hf}$ is a summation of all terms' contribution. Note that no special damping function is needed in practice for point charge or dispersion interactions. The final fitting results for all terms and the total interaction energy are shown in the electronic Supporting Information (ESI), yielding an rms error between the fitted and ab initio interactions energies of only 0.28 mH (0.74 kJ/mol). The final fitted parameters are given in Table 1.

CO_2 Second Virial Coefficient. The second virial coefficients of our CO_2 model were calculated by integrating the Mayer function,[64]

$$B_2(T) = -2\pi \int_0^\infty [\langle e^{-\beta u(r)} \rangle - 1] r^2 \, dr$$

where the average was taken over randomly sampled molecular orientations at a fixed intermolecular separation. The results are shown in Figure 1.

As shown, the unscaled model exhibits B_2 coefficients in excellent agreement with experiment, illustrating that our two-body potential is extremely accurate. However, when applied to the bulk, these ab initio parameters lead to densities that are systematically slightly too high. This trade-off in B_2 and bulk properties has also been observed by Persson et al. and was explained in terms of three body effects.[23] Although our model accounts for polarization, which is a major contribution to many body interactions, three-body dispersion interactions are missing from our model.

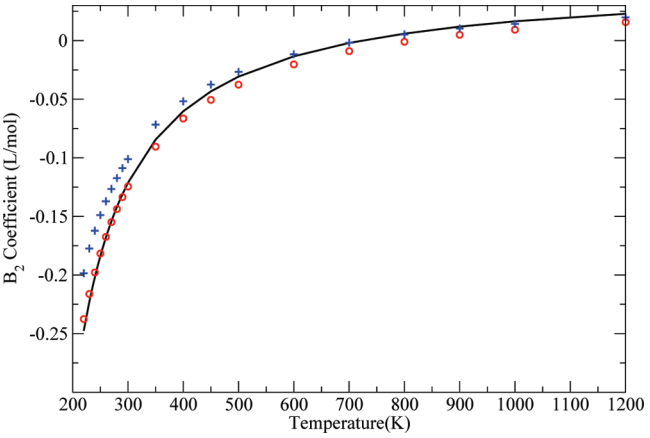

Figure 1. Second virial coefficients for CO_2. Results from unscaled (circle) and scaled (plus) data are shown along with experimental data[65] (solid).

Using a combination of MP2 and HF calculations on CO_2 trimers, we estimated the magnitude of this correction. For both calculations, aug-cc-pVDZ basis was used to accelerate the speed, and BSSE was removed by counterpoise correction. Three-body interaction energies for both MP2 and HF were computed as:

$$\Delta E_{ABC} = E_{ABC} - E_{AB} - E_{BC} - E_{AC} + E_A + E_B + E_C$$

Attributing the difference in the MP2 and HF interaction energies primarily to dispersion, the three-body dispersion is estimated by $\Delta E_{ABC}^{MP2} - \Delta E_{ABC}^{HF}$. Our analysis showed that there is typically a positive energy contribution from three-body dispersion, opposing the negative two-body dispersion contributions. Using this methodology, we would estimate the magnitude of three-body dispersion at typically ~3% of the magnitude of two-body dispersion (thus weakening the dispersive interactions). Motivated by these results, we find that a scaling factor of 0.935 applied to the dispersion energy contribution yields the most accurate bulk densities. Consequently, the scaled potential exhibits somewhat worse agreement with B_2 coefficients in the low temperature region.

Note that this dispersion scale factor is the *only* empirical parameter in this model and is motivated by our explicit trimer calculations and is essentially accounting for three-body dispersion in an average manner. While our scaling factor of 0.935, corresponding to 6.5% correction, is not quantitatively fixed via our timer calculations, these calculations demonstrate that three-body dispersion is an important component for a highly accurate CO_2 force field. To arrive at a force field that is computationally efficient and amenable to popular simulation packages, we employ a mean field treatment of many-body dispersion effects via simple scale factor and utilize this model for all subsequent calculations.

CO_2 Properties in Homogeneous Region. Densities of CO_2 at different points in the phase diagram were computed and compared to experiment, and the results are shown in Figure 2.[65] The densities in a wide range of points are well reproduced by our model, with typical errors less than 2%. The largest errors appear in the low temperature, very high density region, most likely because of the relatively poorer fitting in the highly repulsive potential region.

The structure of liquid CO_2 is benchmarked by comparing the calculated intermolecular scattering function with experiments.[66]

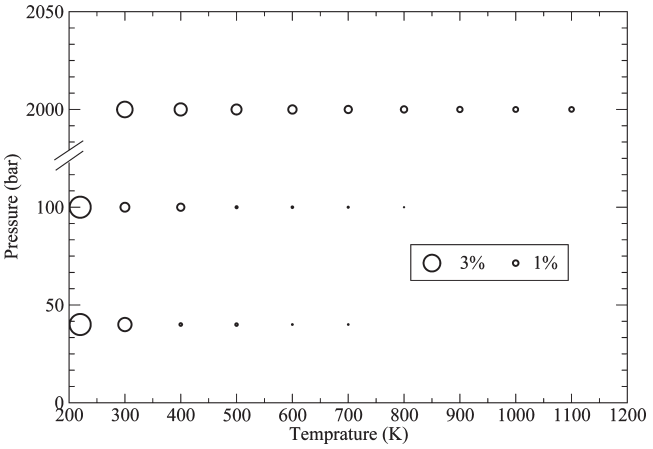

Figure 2. Observed deviation between experimental and model CO_2 densities under a wide variety of conditions.

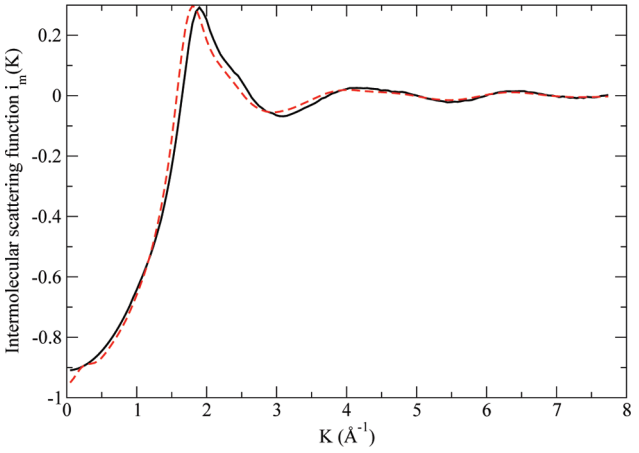

Figure 3. Intermolecular scattering function for liquid CO_2: simulation (red dashed) versus experimental data (black solid).

The simulation is done in the *NPT* ensemble at 239 K and 14.5 bar, mirroring the experimental conditions. The intermolecular scattering function, $i_m(K)$, is calculated by the Fourier transform of the radial distribution function, $g_m(r)$, and the results are shown in Figure 3.[66] A slight shift can be observed in the first peak, while in general the shape of the whole curve is well reproduced.

$$i_m(K) = \frac{4\pi n}{K}\int_0^\infty r(g_m(r) - 1)\sin(Kr)\,dr$$
$$g_m(r) = 0.403g_{OO}(r) + 0.464g_{CO}(r) + 0.133g_{CC}(r)$$

Self-diffusion coefficients are also predicted by MD simulations and compared to experiments[67,68] and are shown in Figure 4. The agreement with experiment is nearly quantitative and as good as newly published empirical models,[22] despite the fact that the present model is essentially parameter free.

The temperature dependence of the CO_2 heat capacity is also computed. A series of *NPT* simulations were conducted at 100 bar and various temperatures, followed by enthalpy calculations based on these simulations. The temperature dependence of the enthalpy is interpolated using cubic splines to generate a smooth curve. Then the numeric derivative was taken from the $H-T$ curve, which is the intermolecular contribution to the isobaric

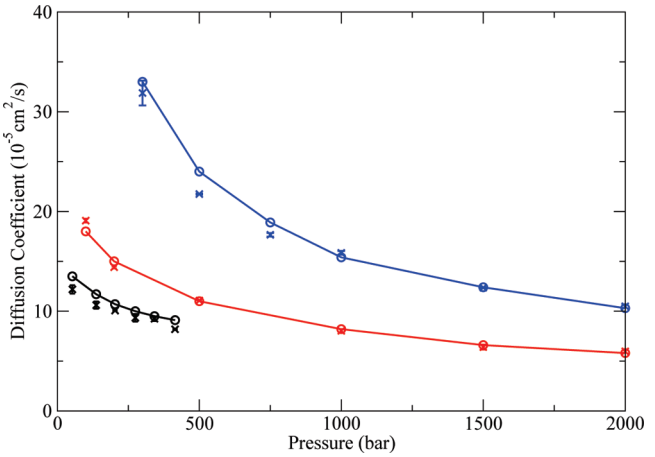

Figure 4. Diffusion coefficients, simulation results (cross) at 273 K (black), 298 K (red), and 373 K (blue) alongside the corresponding experimental results (circle).

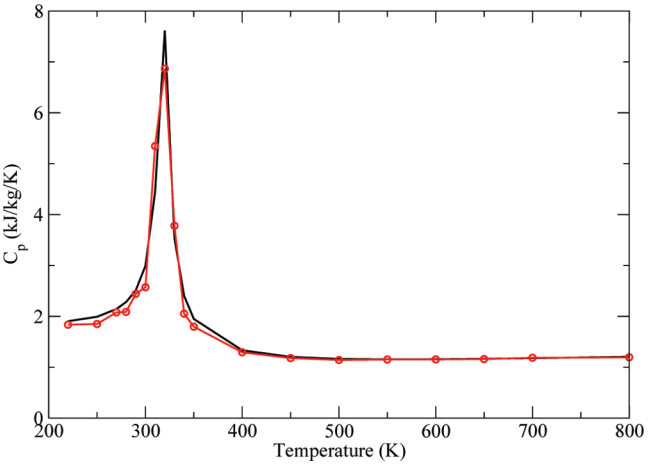

Figure 5. Heat capacity calculated by simulation (red circles) compared to experimental data (black solid).

heat capacity. The intramolecular contribution was computed via the harmonic oscillator approximation:

$$C_p^{\text{intra}} = \sum_i \frac{(h\nu_i/kT)^2 e^{-h\nu_i/kT}}{(1 - e^{-h\nu_i/kT})^2}$$

where i runs over all normal modes of CO_2 and vibration frequencies ν_i were taken from experiment;[69] the results are shown alongside the corresponding experimental values[65] in Figure 5. The peak around 320 K is due to critical phenomenon, which provides a challenging test. Our model accurately predicts the position and the height of this peak and performs excellently in all the other regions, validating the model's thermodynamic performance for properties.

Finally, we performed an energy decomposition for the bulk CO_2 system at various densities and state points. This is the special advantage for our physically motivated force fields: because all the terms were fit individually, the resulting interaction energy is naturally decomposable under conditions of finite temperature and pressure in a standard simulation. One liquid state (300 K/100 bar), one supercritical state (350 K/100 bar), and two gas states (300 K/40 bar and 300 K/10 bar) were tested.

Table 2. Energy Decomposition for Bulk CO_2 in Different Conditions

%	liquid	supercritical	gas/40 bar	gas/10 bar
density (mol/L)	17.916	5.073	1.832	0.422
exchange	−118.9	−110.1	−104.2	−102.2
electrostatic	55.7	50.9	50.7	51.5
dispersion	151.5	148.0	142.7	140.1
induction	7.1	6.8	6.6	6.6
δhf	4.7	4.4	4.1	4.1
total	100.0	100.0	100.0	100.0

Table 2 lists the contribution of the different physical types of interactions by percentage relative to the total interaction potential. Several interesting conclusions can be drawn from these data. First, for the neat CO_2 system, dispersion, exchange, and electrostatic interactions account for approximately 90% of the interaction energy, with induction and the delta Hartree−Fock (higher order effects) playing a less significant role in the total interaction. This likely explains the apparent success of the previous nonpolarizable empirical models. Yet, although the induction contribution is small, it is critical in determining accurate densities; neglecting this term in the total energy yields very significant errors in the observable properties. Previous empirical models must therefore implicitly include this contribution in their Lennard-Jones potential in a mean field fashion. Although this may reproduce neat CO_2 properties, it may not be robust enough in highly polar environments. Second, it can be observed that with decreasing density, the magnitudes of exchange repulsion, dispersion attraction, and induction all decrease, which is consistent with the increasing molecular separations. Third, in the low density limit, with increasing average separation between molecules, the relative contribution from all terms seem to approach constant values. This is somewhat nonintuitive, as one might expect long-range dispersion interactions to become disproportionately dominant in the low density limit. The fact that this is not the case is probably due to the pairwise position correlation between different molecules as the radial distribution function approaches its low-density limit.

CO_2 Vapor−Liquid Equilibrium. The VLE behavior is critical in predicting CO_2 absorption behavior in different types of systems. For various temperatures, vapor phase and liquid phase *NPT* simulations were run at three different pressures around the coexistence pressure. Test particle insertion was used to compute the chemical potentials in these simulations. The resulting $\mu-P$ curves were interpolated to determine the crossing point, P_0, which corresponds to the coexistence pressure for the model. Then *NPT* simulations were run for the two phases at P_0 to determine the respective equilibrium densities. Finally, the supercritical point was obtained by extrapolating the $\rho-T$ curves, utilizing the following equations:[58]

$$\frac{\rho_l + \rho_g}{2} = \rho_c + A(T - T_c)$$
$$\rho_l - \rho_g = B(T - T_c)^{0.32}$$

Figure 6 compares the simulation results to experimental data.[65] It can be seen that, in general, our model predicts very accurate coexistence pressure. The typical error is between 1 and 2 bar, with all values slightly higher than experiment.

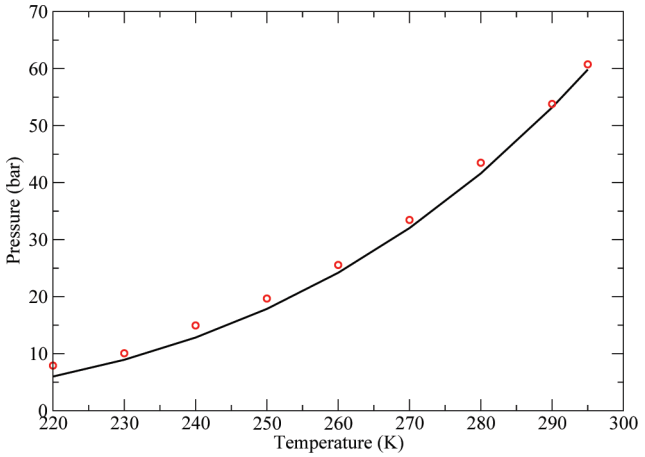

Figure 6. Temperature dependence of vapor−liquid coexistence pressure. Calculated data (circles) are compared with experimental data (solid).

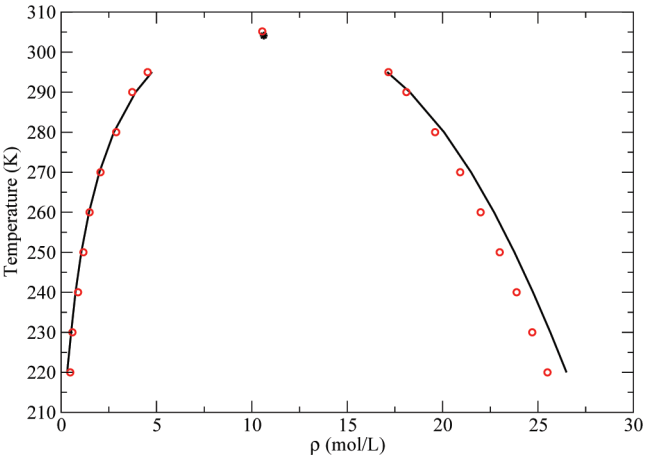

Figure 7. Coexistence density from simulation (circles) compared to experimental data. The two points on the top are the critical points, from our simulation (circle) and experiment (star).

Figure 7 shows the $\rho-T$ phase diagram. The phase behavior is in general well predicted. The critical point from the simulation is 305.17 K, 10.547 mol/L, which is almost identical to the experimental value of 304.13 K and 10.625 mol/L.[22] The major errors in our model occur in the low temperature liquid region, where around a 3% error in the density can be observed, consistent with the deviation that we found in the homogeneous low temperature liquid system.

The enthalpies of vaporization in the coexistence region were also calculated and are available in ESI. Here we find typical discrepancies of approximately 5%, although this error is dominated by the small systematic errors in the coexistence density described above. Correcting for this error by comparing enthalpies calculated at the experimental (rather than model) coexistence densities yields vaporization heats in excellent agreement with experiments, typically less than 2% in error.

N_2 Model Fitting. We also develop an N_2 model, proceeding analogously to the case of CO_2. The molecule is represented by three sites, including two nitrogen atoms and one dummy site (D) at the molecular center of mass. The dummy site interacts only via a partial charge to reproduce the gas phase quadrupole

Table 3. Fitted Parameters for N_2 Molecules[a]

k_{spring} [(kJ/mol)/Å^2]	937.72	
r_{NN} (Å)	1.10	
	D	N
q (e)	0.95904	−0.47952
q_{shell} (e)	–	−0.86920
A^{tot} (kJ/mol) /10^4	–	30.511
B (Å^{-1})	–	3.7842
C [kJ/(mol·Å^{-6})] /10^2	–	14.370
A^{elect} (kJ/mol) /10^4	–	−14.155
A^{exch} (kJ/mol) /10^4	–	48.417
A^{ind} (kJ/mol) /10^4	–	−0.7381
$A^{\delta hf}$ (kJ/mol) /10^4	–	−3.0119

[a] The C coefficient in the table was scaled by 0.940, as explained in the text.

moment; no shell or Buckingham parameters are associated with this dummy site. Like CO_2, N_2 is also a rigid model with r_{NN} = 1.10 Å, close to the experimental value.

It was found that second-order truncated SAPT did not converge to high enough accuracy for the N_2 dimer system, despite its success for the CO_2 dimer. This is likely due to the extremely weak interactions of N_2 molecules, meaning that dispersion must be calculated to extraordinary accuracy. Therefore, we include a CCSD(T) correction, which was calculated by the difference between the CCSD(T) interaction energy and the SAPT total energy and was added to the dispersion term in the SAPT energy decomposition. The fitting scheme was analogous to that used for CO_2 and will not be repeated here. As explained below, it was found that a scaling factor for the dispersion term was also needed for the N_2 molecule. Fitting this scaling factor to B_2 coefficients led to a value of 0.94, which is coincidentally close to the scaling factor for the CO_2 model. However, as we will discuss below, the scaling factors have different physical meanings. Final fittings can be found in ESI, and parameters are listed in Table 3. The rms value of this fitting is 0.094 mH (0.25 kJ/mol).

N_2 Second Virial Coefficients. The second virial coefficient for N_2 was calculated using the same procedure as stated above, and the results are shown in Figure 8. Contrary to what we saw in the analogous CO_2 calculation, where the initial two-body potential was nearly perfect, the unscaled parameters for N_2 give B_2 values that are too negative at low temperatures, meaning the fitted potential is slightly too attractive. This similar phenomenon has also been observed in two previous works that used complicated angular-dependent functional forms to derive an ab initio N_2 dimer potential.[46,47] Thus, we believe that this error originates from the underlying ab initio calculations rather than our fitting procedure.

To verify this assumption, we computed the Mayer function $-2\pi r^2[\langle e^{-\beta u(r)}\rangle - 1]$ using CCSD(T) calculations at three different intermolecular distances. Approximately 800 dimer geometries were randomly sampled at each distance and CCSD(T) calculations were carried out to obtain interaction energies for these geometries, which were used to determine the value of Mayer function. The results are nearly identical to those we determine from our fitted potential, confirming that the source of the discrepancy is not with the fitting, but rather due to insufficiencies in the underlying ab initio calculations. Even though these errors seem to be very small (we estimate around 0.1 mH at

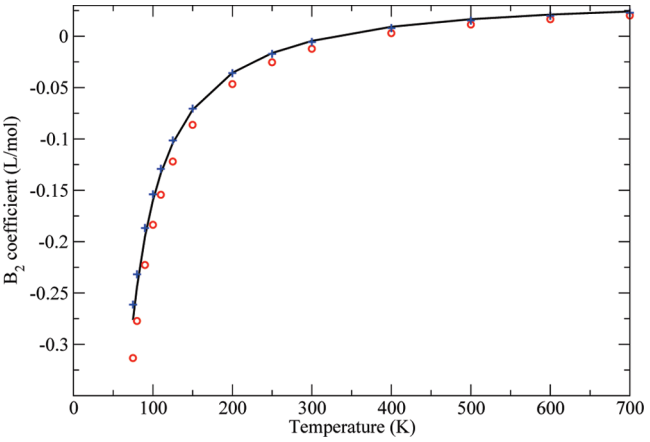

Figure 8. Second virial coefficient for N_2 molecules. Results from unscaled model (circles) and scaled model (plus) are plotted along with experimental data[70] (solid).

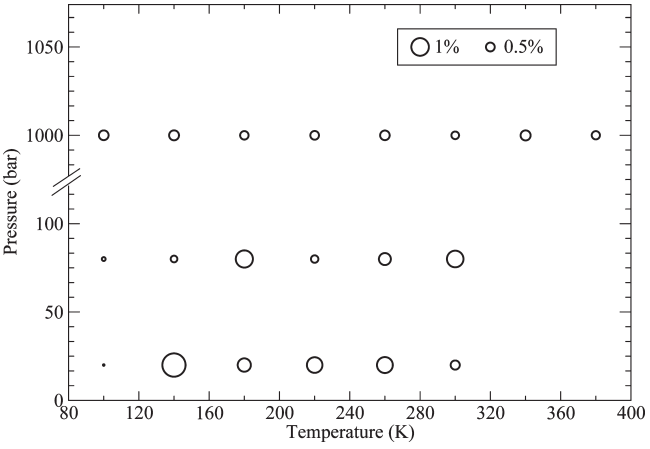

Figure 9. Observed deviation between experimental and model N_2 densities under a wide variety of conditions.

the dimer minimum), they are significant in that the N_2 interactions are very weak, making N_2 properties extraordinarily sensitive to these small errors. Because CCSD(T) is the upper limit of our computational capabilities, we decided to simply use the empirical scaling factor of 0.94 applied to the dispersion energies to correct this two body interaction error, and all subsequent simulations are done with this scaling factor. The scaled parameters also give improved densities compared to the unscaled parameters. Therefore, we do not see the same B_2 coefficient−density trade-off that we saw in CO_2, confirming that the problem lies with the two-body potential. Presumably higher-level coupled cluster calculations accounting for triple and/or quadruple excitations would make such scaling unnecessary.

N_2 Properties in Homogeneous Region. Densities for pure N_2 were tested over a wide range of the phase diagram. The deviations of the density compared to experiments[71] are presented in Figure 9. The deviations are even smaller than those of CO_2, with errors less than 1.5%, with the larger deviations occurring in the high density gas region.

The liquid structure of N_2 was studied by comparing the scattering structure factor with neutron scattering experiments.[72] The *NVT* simulation was conducted at 77.4 K with a density of 28.7 mol/L, mimicking experimental conditions. The total

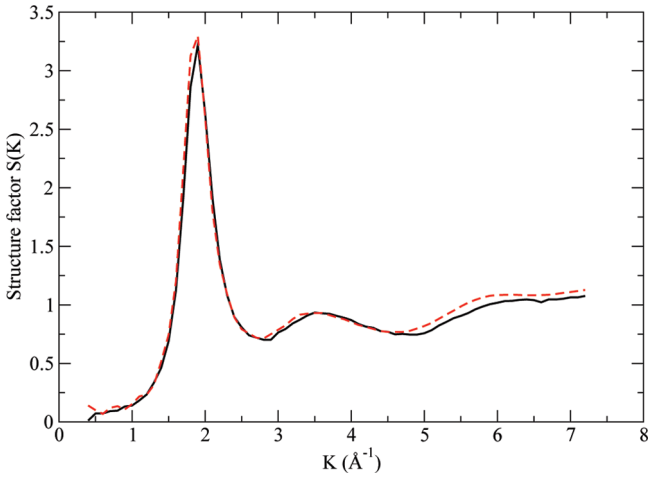

Figure 10. Structure factor for liquid nitrogen. Calculated curve (red dashed) is plotted with experimental curve (black solid).

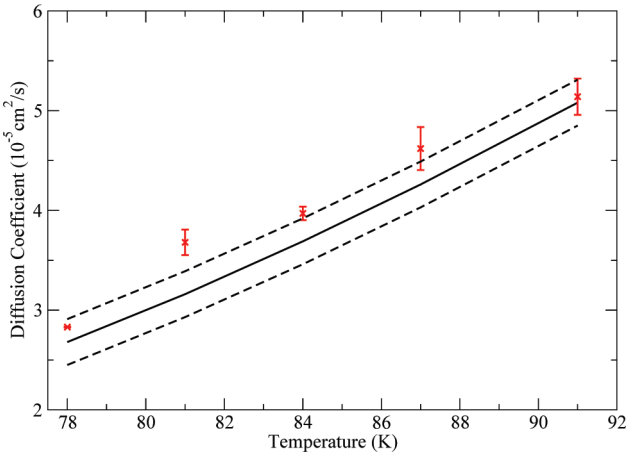

Figure 11. N_2 diffusion coefficients along vapor−liquid coexistence line. Simulation results (red cross) are plotted along with the empirical equation (black solid) fit to experimental values and the corresponding estimated experimental uncertainty (black dashed).

structure factor has contributions from both inter- and intramolecular parts, and was calculated using[73]

$$S(K) = 1 + \frac{\sin Kd}{Kd} + S_m(K)$$

Here d is the nitrogen−nitrogen bond length, fixed at 1.10 Å, and $S_m(K)$ is the intermolecular contribution, which was calculated by the Fourier transform of the radial distribution function. Figure 10 plots the simulation and experimental results, yielding essentially quantitative agreement.

Diffusion coefficients were also examined at various points along the vapor−liquid coexistence line. Results are compared with an empirical equation derived from experimental data[74] and are presented in Figure 11. Note that the experiment was done with ^{15}N instead of ^{14}N. However, the differences of diffusion coefficients between these two species are small relative to the uncertainties of experimental data and our simulation results. The agreement between our simulations and experiment is excellent considering the uncertainty of the experimental data.

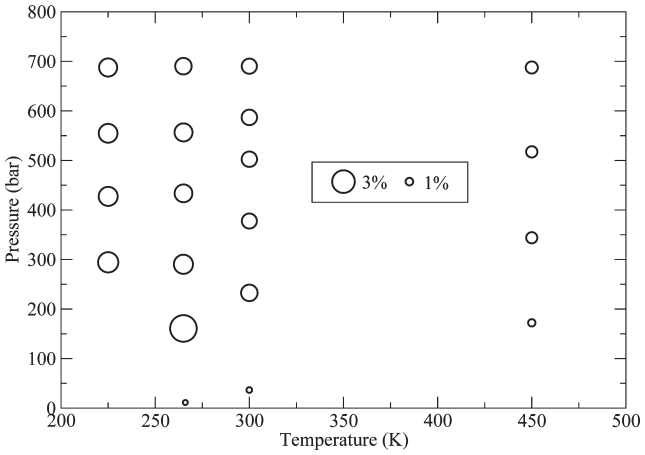

Figure 12. Deviations of the calculated CO_2/N_2 mixture for mixture densities compared to the corresponding experimental densities over a wide variety of conditions.

We note that VLE data for N_2 were not calculated because it is somewhat computationally demanding and of significantly less interest as compared to CO_2.

Mixture Properties. In addition to the properties of neat CO_2 and N_2, we also benchmarked mixture properties due to their relevance in many technological and industrial applications. SAPT calculations were done between CO_2 and N_2 for comparison. Cross terms for CO_2 and N_2 interactions were not fit but rather determined by simple combination rule for regular Buckingham potential based on the parameters for the total interaction potential of CO_2 and N_2,

$$A_{ij} = \sqrt{A_{ii}A_{jj}}$$
$$B_{ij} = 2/(1/B_{ii} + 1/B_{jj})$$
$$C_{ij} = \sqrt{C_{ii}C_{jj}}$$

In ESI, the comparison between our classical model using the combination rule and SAPT interaction energies can be found. The comparison is quite good with an rms error of only 0.3 mH (0.79 kJ/mol), essentially the same as for neat CO_2, confirming the robustness and physical nature of our parameters. Although small, the error in the cross terms is systematically too repulsive, probably due to the scaling factor that we used for the CO_2 force field. Given these promising results, we directly utilize the combination rules to simulate properties of the bulk mixtures.

The densities of mixtures were calculated and compared to the experimental data.[75] These mixtures were studied at a variety of temperatures, pressures, and the molar ratios of CO_2. Results for various molar ratios are rather similar, and the deviations of densities in the molar ratio of 0.503 are illustrated in Figure 12. Excellent agreement is obtained, comparable with that of the pure CO_2 system, again confirming the robustness of this force field.

Model Performance. The polarizable shell model adopted in this work is more computationally intensive than traditional nonpolarizable point charge models like EPM2 or TraPPE, primarily due to the self-consistent iterations required at each time step. Although this limitation can be mitigated via sophisticated techniques such as a predictor corrector method[76] or extended Lagrangian approaches,[77] we have not yet attempted to implement these methodologies. While these methods are

inapplicable to Monte Carlo simulation methods, they would be a promising alternative in MD simulations to accelerate significantly the speed. We have also parametrized our model for use with long cutoffs (14 Å for real space electrostatics and 15 Å for Buckingham potential were used in all simulations) to ensure that all structure in the radial distribution function has vanished prior to the application of long-range corrections. However, we note that with long-range correction these cutoffs can be decreased to 10 Å for real space electrostatics and 11 Å for Buckingham potential without any significant change in the potential and density, and approximately doubling the simulation speed. Thus, even in a naïve implementation, our present model is only approximately 1 order of magnitude slower than the simplest empirical model. Furthermore, the standard form of the potential means that the model can be implemented in most standard molecular simulation packages that support shell polarization (such as Gromacs) without modification.

CONCLUSIONS

A physically motivated, first-principles based polarizable force field was developed for CO_2 and N_2. Exchange, electrostatic, induction and dispersion interaction parameters were fit to individual components of SAPT dimer energy calculations. The resulting CO_2 and N_2 force field was benchmarked against experimental data for various types of properties, including the second virial coefficient, density, scattering structure factor, heat capacity and vapor−liquid coexistence curves. In general, excellent agreement with experimental data was obtained with our model.

Our force field is novel in that it utilizes the natural energy decomposition of SAPT to explicitly partition the classical interaction energy into physically distinct terms. This allows for trivial energy decomposition in bulk simulations, enabling more physical insight than that provided with widely used empirical models. More importantly, the "physical" nature of the force field suggests that the results should be robust, yielding the right answer, for the right reason, without relying on a subtle cancellation of errors. We would expect that this robustness would manifest itself in many ways, including the transferability of the model to novel environments for which it was not explicitly parametrized, particularly if the remainder of the system has been parametrized in a similarly "physical" manner.

Here, we provide one explicit illustration of this transferability, looking at the properties of CO_2 and N_2 mixtures. Using simple combination rules in the absence of additional parametrization, we find not only good agreement with SAPT mixed-dimer calculations but also accurate description of bulk mixtures, evidencing the robustness of the methodology. As such, we anticipate that these models will be extremely useful particularly for examining interactions of CO_2 and N_2 with complex solid and liquid media, where traditional empirical, nonpolarizable force fields are likely to fail.

ASSOCIATED CONTENT

Supporting Information. Figure of the final fitting results for CO_2-CO_2 exchange energy; figure of the final fitting results for CO_2-CO_2 electrostatic energy; figure of the final fitting results for CO_2-CO_2 induction energy; figure of the final fitting results for CO_2-CO_2 dispersion energy; figure of the final fitting results for CO_2-CO_2 δHF energy; figure of the final fitting results for CO_2-CO_2 total interaction energy; figure of the final fitting results for N_2-N_2 exchange energy; figure of the final fitting results for N_2-N_2 electrostatic energy; figure of the final fitting results for N_2-N_2 induction energy; figure of the final fitting results for N_2-N_2 dispersion energy; figure of the final fitting results for N_2-N_2 δHF energy; figure of the final fitting results for N_2-N_2 total interaction energy; figure of the CO_2-N_2 total interaction energy comparison; table of the second virial coefficients for CO_2; table of the diffusion coefficient for CO_2; table of the CO_2 VLE data; table of the second virial coefficients for N_2; table of the diffusion coefficients for N_2. This material is available free of charge via the Internet at http://pubs.acs.org.

AUTHOR INFORMATION

Corresponding Author
*E-mail: schmidt@chem.wisc.edu.

ACKNOWLEDGMENT

We thank Arun Yethiraj for many helpful discussions. This research was supported by the National Science Foundation through TeraGrid resources provided by Purdue University and via grant CHE-0840494.[78] Additional computing resources were provided via the Center for High Throughput Computing at the University of Wisconsin.[79] This research was supported by DOE (DE-FG02-09ER16059).

REFERENCES

(1) Intergovernmental Panel on Climate Change. *Carbon Dioxide Capture and Storage*; Davidson, O., de Coninck, H., Eds.; Cambridge University Press: Cambridge, U.K., 2005.
(2) Phan, A.; Doonan, C. J.; Uribe-Romo, F. J.; Knobler, C. B.; O'Keeffe, M.; Yaghi, O. M. *Acc. Chem. Res.* **2009**, *43*, 58.
(3) Demessence, A.; D'Alessandro, D. M.; Foo, M. L.; Long, J. R. *J. Am. Chem. Soc.* **2009**, *131*, 8784.
(4) Gurkan, B.; Goodrich, B. F.; Mindrup, E. M.; Ficke, L. E.; Massel, M.; Seo, S.; Senftle, T. P.; Wu, H.; Glaser, M. F.; Shah, J. K.; Maginn, E. J.; Brennecke, J. F.; Schneider, W. F. *J. Phys. Chem. Lett.* **2010**, *1*, 3494.
(5) Gurkan, B. E.; de la Fuente, J. C.; Mindrup, E. M.; Ficke, L. E.; Goodrich, B. F.; Price, E. A.; Schneider, W. F.; Brennecke, J. F. *J. Am. Chem. Soc.* **2010**, *132*, 2116.
(6) Wick, C. D.; Chang, T. M.; Dang, L. X. *J. Phys. Chem. B* **2010**, *114*, 14965.
(7) Yazaydin, A. O.; Snurr, R. Q.; Park, T.-H.; Koh, K.; Liu, J.; LeVan, M. D.; Benin, A. I.; Jakubczak, P.; Lanuza, M.; Galloway, D. B.; Low, J. J.; Willis, R. R. *J. Am. Chem. Soc.* **2009**, *131*, 18198.
(8) Liu, B.; Smit, B. *J. Phys. Chem. C* **2010**, *114*, 8515.
(9) Gibbons, T. G.; Klein, M. L. *J. Chem. Phys.* **1974**, *60*, 112.
(10) Macrury, T. B.; Steele, W. A.; Berne, B. J. *J. Chem. Phys.* **1976**, *64*, 1288.
(11) Murphy, W. F.; Montero, S. *Mol. Phys.* **1981**, *44*, 187.
(12) Murthy, C. S.; Oshea, S. F.; Mcdonald, I. R. *Mol. Phys.* **1983**, *50*, 531.
(13) Galassi, G.; Tildesley, D. J. *Mol. Simul.* **1994**, *13*, 11.
(14) Kuchta, B.; Etters, R. D. *Phys. Rev. B* **1988**, *38*, 6265.
(15) Etters, R. D.; Kuchta, B. *J. Chem. Phys.* **1989**, *90*, 4537.
(16) Moller, D.; Fischer, J. *Fluid Phase Equilib.* **1994**, *100*, 35.
(17) Harris, J. G.; Yung, K. H. *J. Phys. Chem.* **1995**, *99*, 12021.
(18) Potoff, J. J.; Siepmann, J. I. *AIChE J.* **2001**, *47*, 1676.
(19) Vrabec, J.; Stoll, J.; Hasse, H. *J. Phys. Chem. B* **2001**, *105*, 12126.
(20) Zhang, Z. G.; Duan, Z. H. *J. Chem. Phys.* **2005**, 122.
(21) Zhu, A. M.; Zhang, X. B.; Liu, Q. L.; Zhang, Q. G. *Chin. J. Chem. Eng.* **2009**, *17*, 268.

(22) Merker, T.; Engin, C.; Vrabec, J.; Hasse, H. *J. Chem. Phys.* **2010**, *132*, 034312.
(23) Persson, R. A. X. *J. Chem. Phys.* **2011**, *134*, 034312.
(24) Domanski, K. B.; Kitao, O.; Nakanishi, K. *Mol. Simul.* **1994**, *12*, 343.
(25) Welker, M.; Steinebrunner, G.; Solca, J.; Huber, H. *Chem. Phys.* **1996**, *213*, 253.
(26) Steinebrunner, G.; Dyson, A. J.; Kirchner, B.; Huber, H. *J. Chem. Phys.* **1998**, *109*, 3153.
(27) Bock, S.; Bich, E.; Vogel, E. *Chem. Phys.* **2000**, *257*, 147.
(28) Tsuzuki, S.; Uchimaru, T.; Mikami, M.; Tanabe, K.; Sako, T.; Kuwajima, S. *Chem. Phys. Lett.* **1996**, *255*, 347.
(29) Tsuzuki, S.; Uchimaru, T.; Tanabe, K.; Kuwajima, S.; Tajima, N.; Hirano, T. *J. Phys. Chem.* **1996**, *100*, 4400.
(30) Bukowski, R.; Sadlej, J.; Jeziorski, B.; Jankowski, P.; Szalewicz, K. *J. Chem. Phys.* **1999**, *110*, 3785.
(31) Williams, H. L.; Chabalowski, C. F. *J. Phys. Chem. A* **2001**, *105*, 646.
(32) Hesselmann, A.; Jansen, G. *Chem. Phys. Lett.* **2002**, *357*, 464.
(33) Hesselmann, A.; Jansen, G. *Chem. Phys. Lett.* **2002**, *362*, 319.
(34) Hesselmann, A.; Jansen, G. *Chem. Phys. Lett.* **2003**, *367*, 778.
(35) Hesselmann, A.; Jansen, G. *Phys. Chem. Chem. Phys.* **2003**, *5*, 5010.
(36) Hesselmann, A.; Jansen, G.; Schutz, M. *J. Chem. Phys.* **2005**, 122.
(37) Everitt, K. F.; Skinner, J. L. *J. Chem. Phys.* **2001**, *115*, 8531.
(38) Johnson, J. D.; Shaw, M. S.; Holian, B. L. *J. Chem. Phys.* **1984**, *80*, 1279.
(39) Aquilanti, V.; Bartolomei, M.; Cappelletti, D.; Carmona-Novillo, E.; Pirani, F. *J. Chem. Phys.* **2002**, *117*, 615.
(40) Goharshadi, E. K.; Abbaspour, M.; Jorabchi, M. N.; Nahali, M. *Chem. Phys.* **2009**, *358*, 185.
(41) Jordan, P. C.; Van Maaren, P. J.; Mavri, J.; Van Der Spoel, D.; Berendsen, H. J. C. *J. Chem. Phys.* **1995**, *103*, 2272.
(42) Berns, R. M.; Vanderavoird, A. *J. Chem. Phys.* **1980**, *72*, 6107.
(43) Vanderavoird, A.; Wormer, P. E. S.; Jansen, A. P. J. *J. Chem. Phys.* **1986**, *84*, 1629.
(44) Stallcop, J. R.; Partridge, H. *Chem. Phys. Lett.* **1997**, *281*, 212.
(45) Strak, P.; Krukowski, S. *J. Chem. Phys.* 2007, *126*.
(46) Gomez, L.; Bussery-Honvault, B.; Cauchy, T.; Bartolomei, A.; Cappelletti, D.; Pirani, F. *Chem. Phys. Lett.* **2007**, *445*, 99.
(47) Cappelletti, D.; Pirani, F.; Bussery-Honvault, B.; Gomez, L.; Bartolomei, M. *Phys. Chem. Chem. Phys.* **2008**, *10*, 4281.
(48) Bartolomei, M.; Carmona-Novillo, E.; Hernandez, M. I.; Campos-Martinez, J.; Hernandez-Lamoneda, R. *J. Comput. Chem.* **2011**, *32*, 279.
(49) Werner, H.-J.; Knowles, P. J.; Lindh, R.; Manby, F. R.; Schutz, M.; Celani, P.; Korona, T.; Mitrushenkov, A.; Rauhut, G.; Adler, T. B.; Amos, R. D.; Bernhardsson, A.; Berning, A.; Cooper, D. L.; Deegan, M. J. O.; Dobbyn, A. J.; Eckert, F.; Goll, E.; Hampel, C.; Hetzer, G.; Hrenar, T.; Knizia, G.; Köppl, C.; Liu, Y.; Lloyd, A. W.; Mata, R. A.; May, A. J.; McNicholas, S. J.; Meyer, W.; Mura, M. E.; Nicklass, A.; Palmieri, P.; Pfluger, K.; Pitzer, R.; Reiher, M.; Schumann, U.; Stoll, H.; Stone, A. J.; Tarroni, R.; Thorsteinsson, T.; Wang, M.; Wolf, A. *MOLPRO, a package of ab initio programs*, version 2009.1; see http://www.molpro.net.
(50) Perdew, J. P.; Burke, K.; Ernzerhof, M. *Phys. Rev. Lett.* **1996**, *77*, 3865.
(51) Perdew, J. P.; Burke, K.; Ernzerhof, M. *Phys. Rev. Lett.* **1997**, *78*, 1396.
(52) Gruning, M.; Gritsenko, O. V.; van Gisbergen, S. J. A.; Baerends, E. J. *J. Chem. Phys.* **2001**, *114*, 652.
(53) Williams, H. L.; Mas, E. M.; Szalewicz, K.; Jeziorski, B. *J. Chem. Phys.* **1995**, *103*, 7374.
(54) Hess, B.; Kutzner, C.; van der Spoel, D.; Lindahl, E. *J. Chem. Theory Comput.* **2008**, *4*, 435.
(55) http://towhee.sourceforge.net/.
(56) Lindan, P. J. D.; Gillan, M. J. *J. Phys.: Condens. Matter* **1993**, *5*, 1019.
(57) Cracknell, R. F.; Nicholson, D.; Parsonage, N. G.; Evans, H. *Mol. Phys.* **1990**, *71*, 931.
(58) Frenkel, D.; Smit, B. *Understanding Molecular Simulation, from algorithms to applications*, 2nd ed.; Academic Press: New York, 2001.
(59) Rick, S. W.; Stuart, S. J. *Rev. Comput. Chem.* **2002**, *18*, 89.
(60) Thole, B. T. *Chem. Phys.* **1981**, *59*, 341.
(61) Yu, H. B.; Whitfield, T. W.; Harder, E.; Lamoureux, G.; Vorobyov, I.; Anisimov, V. M.; MacKerell, A. D.; Roux, B. *J. Chem. Theory Comput.* **2010**, *6*, 774.
(62) Lewis, M.; Wu, Z. Y.; Glaser, R. *J. Phys. Chem. A* **2000**, *104*, 11355.
(63) Levy, M.; Perdew, J. P.; Sahni, V. *Phys. Rev. A* **1984**, *30*, 2745.
(64) McQuarrie, D. A. *Statistical Mechanics*, 1st ed.; University Science Books: South Orange, NJ, 2000.
(65) Span, R.; Wagner, W. *J. Phys. Chem. Ref. Data* **1996**, *25*, 1509.
(66) Vantricht, J. B.; Fredrikze, H.; Vanderlaan, J. *Mol. Phys.* **1984**, *52*, 115.
(67) Etesse, P.; Zega, J. A.; Kobayashi, R. *J. Chem. Phys.* **1992**, *97*, 2022.
(68) Gross, T.; Buchhauser, J.; Ludemann, H. D. *J. Chem. Phys.* **1998**, *109*, 4518.
(69) Herzberg, G. *Molecular spectra and molecular structure*, 2nd ed.; Reitell Press: Davison, MI, 2008; Vol. 2.
(70) Ewing, M. B.; Trusler, J. P. M. *Physica A* **1992**, *184*, 415.
(71) http://webbook.nist.gov/chemistry/. NIST Chemistry WebBook; NIST: Washington, DC.
(72) Dore, J. C.; Walford, G.; Page, D. I. *Mol. Phys.* **1975**, *29*, 565.
(73) Cheung, P. S. Y.; Powles, J. G. *Mol. Phys.* **1975**, *30*, 921.
(74) Krynicki, K.; Rahkamaa, E. J.; Powles, J. G. *Mol. Phys.* **1974**, *28*, 853.
(75) Brugge, H. B.; Holste, J. C.; Hall, K. R.; Gammon, B. E.; Marsh, K. N. *J. Chem. Eng. Data* **1997**, *42*, 903.
(76) Sala, J.; Guardia, E.; Masia, M. *J. Chem. Phys.* **2010**, 133.
(77) Andersen, H. C. *J. Chem. Phys.* **1980**, *72*, 2384.
(78) *TeraGrid: Analysis of Organization, System Architecture, and Middleware Enabling New Types of Applications*; Catlett, C., Ed.; IOS Press: Amsterdam, 2007.
(79) Litzkow, M.; Livny, M.; Mutka, M. Condor - A Hunter of Idle Workstations. *8th International Conference of Distributed Computing Systems*; IEEE: New York, 1988.